Pygmy dipole strength in ^{86}Kr and systematics of $N = 50$ isotones

R. Schwengner,[1] R. Massarczyk,[1,2] G. Rusev,[3,4,*] N. Tsoneva,[5,6] D. Bemmerer,[1] R. Beyer,[1] R. Hannaske,[1,2] A. R. Junghans,[1] J. H. Kelley,[4,7] E. Kwan,[3,4,†] H. Lenske,[5] M. Marta,[1,‡] R. Raut,[3,4,§] K. D. Schilling,[1] A. Tonchev,[3,4,†] W. Tornow,[3,4] and A. Wagner[1]

[1]*Institut für Strahlenphysik, Helmholtz-Zentrum Dresden-Rossendorf, 01314 Dresden, Germany*
[2]*Technische Universität Dresden, 01062 Dresden, Germany*
[3]*Department of Physics, Duke University, Durham, North Carolina 27708, USA*
[4]*Triangle Universities Nuclear Laboratory, Durham, North Carolina 27708, USA*
[5]*Institut für Theoretische Physik, Universität Gießen, 35392 Gießen, Germany*
[6]*Institute for Nuclear Research and Nuclear Energy, BAS, 1784 Sofia, Bulgaria*
[7]*Department of Physics, North Carolina State University, Raleigh, North Carolina 27695, USA*

(Received 26 November 2012; published 8 February 2013)

The dipole strength of the $N = 50$ nucleus ^{86}Kr was studied in photon-scattering experiments using bremsstrahlung produced with electron beams of energies of 7.9 and 11.2 MeV delivered by the linear accelerator ELBE as well as using quasimonoenergetic and linearly polarized γ rays of 10 energies within the range from 4.7 to 9.3 MeV delivered by the HIγS facility. A high-pressure gas target was used. We identified 39 levels up to an excitation energy of 10.1 MeV. Simulations of γ-ray cascades were performed to estimate intensities of inelastic transitions and to correct the intensities of the ground-state transitions for their branching ratios. The photoabsorption cross section derived in this way up to the neutron-separation energy is combined with the photoabsorption cross section obtained from a (γ, n) experiment at HIγS. The enhanced $E1$ strength found in the range from 6 to 10 MeV is compared with the ones in the $N = 50$ isotones ^{88}Sr, ^{90}Zr, and ^{92}Mo and with predictions of calculations within the quasiparticle-phonon model.

DOI: 10.1103/PhysRevC.87.024306 PACS number(s): 25.20.Dc, 21.60.Jz, 23.20.−g, 27.50.+e

I. INTRODUCTION

Gamma-ray strength functions, in particular electric dipole ($E1$) and magnetic dipole ($M1$) strength functions, are an important ingredient for the calculation of rates of photonuclear reactions as well as of the inverse radiative-capture reactions on the basis of statistical reaction models. Radiative neutron capture, for example, is an important reaction for the synthesis of heavy nuclei in stellar environments. Moreover, an improved experimental and theoretical description of neutron capture is important for next-generation nuclear technologies, such as transmutation of nuclear waste.

The dipole strength function f_1 is connected with the photoabsorption cross section σ_γ via the relation $f_1 = \sigma_\gamma/[g(\pi\hbar c)^2 E_\gamma]$ with $g = (2J_i + 1)/(2J_0 + 1)$, where J_0 and J_i are the spins of the ground state and the excited state, respectively. At high excitation energy above the neutron-separation energy S_n, the photoabsorption cross section is dominated by the isovector giant dipole resonance (GDR) observable in (γ, n) experiments. To approximate the shape of the GDR, σ_γ has been phenomenologically described by a standard Lorentz curve (SLO) [1,2] or by a generalized Lorentz curve (GLO) including terms taking into account nuclear temperature [2–4]. Double humps or a widening of the GDR caused by quadrupole and triaxial deformation of the nuclei can be reproduced with combinations of two or three Lorentz curves [5,6], which are adjusted to (γ, n) data [2]. An alternative description [7] uses the energies of a triaxial oscillator for the centroids of the three Lorentz curves and a global expression for the widths [8,9] instead of an adjustment to individual (γ, n) data.

A special feature under discussion for a long time [10] is enhanced strength that is observed in the low-energy tail of the GDR. This strength reflects nuclear structure properties and is often referred to as the pygmy dipole resonance (PDR). In the framework of the quasiparticle random-phase approximation (QRPA) this PDR has been ascribed to an oscillation of excessive neutrons versus the symmetric ($N = Z$) neutron-proton system [11–14]. Recent experiments may indicate that the PDR splits into a low-lying isoscalar component and a higher-lying more isovector component [15].

Photon scattering from nuclei, also called nuclear resonance fluorescence (NRF), is an ideal tool to study dipole strength functions below S_n because predominantly states with spin $J = 1$ and, to a lesser extent, states with $J = 2$ are excited from the ground state in an even-even nucleus. NRF experiments allow an unambiguous determination of σ_γ and f_1 on an absolute scale.

We have performed systematic studies of dipole strength distributions up to S_n for varying neutron numbers in the chain of stable even-mass Mo isotopes [16,17] and for varying proton numbers in the chain of stable $N = 50$ isotones [18–20] by

*Present address: Chemistry Division, Los Alamos National Laboratory, Los Alamos, New Mexico 87545, USA.
†Present address: Physics Division, Lawrence Livermore National Laboratory, Livermore, California 94550, USA.
‡Present address: GSI Helmholtzzentrum für Schwerionenforschung, 64291 Darmstadt, Germany.
§Present address: UGC-DAE Consortium for Scientific Research, Kolkata Centre LB-8 Sector-III Bidhannagar, Kolkata 700098, India.

means of photon scattering using the bremsstrahlung facility [21] at the superconducting electron accelerator ELBE [22,23] of the Helmholtz-Zentrum Dresden-Rossendorf (HZDR).

The present work describes the first photon-scattering study of the lightest stable $N = 50$ isotone ^{86}Kr. We performed experiments with bremsstrahlung at ELBE as well as with monoenergetic γ radiation at the High-Intensity γ-ray Source (HIγS) [24] operated by the Triangle Universities Nuclear Laboratory (TUNL). We identified 39 levels up to 10.1 MeV and assigned spins and parities to most of them. We performed simulations of γ-ray cascades to estimate intensities of inelastic transitions to low-lying excited levels in the experiments with bremsstrahlung. The dipole strength distribution deduced for ^{86}Kr from the present experiments is compared with the ones in the other stable even-even $N = 50$ isotones and with predictions of the quasiparticle-phonon model (QPM).

II. EXPERIMENTAL METHODS AND RESULTS

A. The photon-scattering method

In photon-scattering experiments, the energy- and solid-angle-integrated scattering cross section I_s of an excited state at energy E_x can be deduced from the measured intensity of the respective transition to the ground state. It can be determined relative to known integrated scattering cross sections. In the present experiments, we used the integrated scattering cross sections $I_s(E_x^{\mathrm{B}})$ of states in ^{11}B [25] and their angular correlations including mixing ratios [26] as a reference:

$$\frac{I_s(E_x)}{I_s\left(E_x^{\mathrm{B}}\right)} = \left(\frac{I_\gamma(E_\gamma,\theta)}{W(E_\gamma,\theta)\Phi_\gamma(E_x)N_N}\right) \times \left(\frac{I_\gamma\left(E_\gamma^{\mathrm{B}},\theta\right)}{W\left(E_\gamma^{\mathrm{B}},\theta\right)\Phi_\gamma\left(E_x^{\mathrm{B}}\right)N_N^{\mathrm{B}}}\right)^{-1}. \quad (1)$$

Here, $I_\gamma(E_\gamma,\theta)$ and $I_\gamma(E_\gamma^{\mathrm{B}},\theta)$ denote the measured intensities of a considered ground-state transition at E_γ and of a ground-state transition in ^{11}B at E_γ^{B}, respectively, observed at an angle θ to the beam. $W(E_\gamma,\theta)$ and $W(E_\gamma^{\mathrm{B}},\theta)$ describe the angular correlations of these transitions. The quantities N_N and N_N^{B} are the numbers of nuclei in the ^{86}Kr and ^{11}B targets, respectively. The quantities $\Phi_\gamma(E_x)$ and $\Phi_\gamma(E_x^{\mathrm{B}})$ stand for the photon fluxes at the energy of the considered level and at the energy of a level in ^{11}B, respectively.

The integrated scattering cross section is related to the partial width of the ground-state transition Γ_0 according to

$$I_s = \int \sigma_{\gamma\gamma}\,dE = \left(\frac{\pi\hbar c}{E_x}\right)^2 \frac{2J_x+1}{2J_0+1}\frac{\Gamma_0^2}{\Gamma}, \quad (2)$$

where $\sigma_{\gamma\gamma}$ is the elastic scattering cross section, E_x, J_x, and Γ denote energy, spin, and total width of the excited level, respectively, and J_0 is the spin of the ground state.

The determination of the level widths is complicated by two problems. First, a considered level can be fed by transitions from higher-lying states; second, a considered level can deexcite to low-lying excited states (inelastic scattering) in addition to the deexcitation to the ground state (elastic scattering). In the case of feeding, the measured intensity of the ground-state transition is greater than the one resulting from a direct excitation only. As a consequence, the integrated scattering cross section I_{s+f} deduced from this intensity contains a portion I_f originating from feeding in addition to the true integrated scattering cross section I_s. In the case of inelastic scattering, inelastic and subsequent cascade transitions appear in the measured spectrum in addition to ground-state transitions. To deduce the partial width of a ground-state transition Γ_0 and the absorption cross section one needs to know the branching ratio $b_0 = \Gamma_0/\Gamma$.

Spins of excited states can be deduced by comparing experimental ratios of intensities, measured at two angles, with theoretical predictions. The optimum combination are angles of 90° and 127° because the respective ratios for the spin sequences 0–1–0 and 0–2–0 differ most at these angles. The expected values are $W(90°)/W(127°)_{0\text{–}1\text{–}0} = 0.74$ and $W(90°)/W(127°)_{0\text{–}2\text{–}0} = 2.18$ by taking into account opening angles of 16° and 14° of the detectors placed at 90° and 127°, respectively, in the setup at ELBE.

B. The target

The target used was a high-pressure gas target as described in Ref. [27]. The spherical container made of stainless steel with an inner diameter of 20 mm and a wall thickness of 0.5 mm contained 1012.6 mg of Kr enriched to 99.41% in ^{86}Kr. In the experiments at ELBE, the ^{86}Kr target was combined with 150.5 mg of ^{11}B, enriched to 99.5% and shaped into a disk of 20 mm in diameter, to determine the photon flux from known scattering cross sections of levels in ^{11}B.

C. Detector response

For the determination of the integrated scattering cross sections according to Eq. (1) the relative efficiencies of the detectors and the relative photon flux are needed. The determination of the absorption cross section described in Sec. III requires a correction of the experimental spectrum for detector response, for the absolute efficiency and the absolute photon flux, for atomic processes induced by the impinging photons in the target material, and for ambient background radiation. The detector response was simulated using the program package GEANT4 [28]. The reliability of the simulation was tested by comparing simulated spectra with measured ones as described in Refs. [16,18,29].

The absolute efficiencies of the HPGe detectors in the setup at ELBE were determined experimentally up to 2.4 MeV from measurements with ^{137}Cs, ^{154}Eu, and ^{226}Ra calibration sources. For interpolation, an efficiency curve calculated with GEANT4 and scaled to the absolute experimental values was used. A check of the simulated efficiency curve up to about 9 MeV was performed via various (p,γ) reactions at the HZDR Tandetron accelerator up to about 9 MeV. The efficiency values deduced from these measurements agree with the simulated values within their uncertainties [30]. Similar results were obtained for the resonances at 4.44 and 11.66 MeV in ^{12}C populated in the ^{11}B(p,γ) reaction at the TUNL van de Graaf accelerator [31].

D. Experiments with bremsstrahlung at ELBE

The nuclide ^{86}Kr was studied in two experiments at ELBE. Bremsstrahlung was produced using electron beams with kinetic energy of 7.9 and 11.2 MeV. The average currents were about 550 μA in the measurement at 7.9 MeV and about 720 μA in the measurement at 11.2 MeV. The electron beams hit a niobium foil of 7 μm thickness acting as a radiator. A 10-cm-thick aluminum absorber was placed behind the radiator to reduce the low-energy part of the bremsstrahlung spectrum (beam hardener). The photon beam, collimated by a 2.6-m-long pure-aluminum collimator with a conical borehole of 8 mm in diameter at the entrance and 24 mm in diameter at the exit, impinged onto the target with a flux of about 10^9 s^{-1} in a spot of 38 mm in diameter. Scattered photons were measured with four high-purity germanium (HPGe) detectors that have an efficiency of 100% relative to a NaI detector of 7.6 cm in diameter and 7.6 cm in length. All HPGe detectors were surrounded by escape-suppression shields made of bismuth germanate (BGO) scintillation detectors of 3 cm in thickness. Two HPGe detectors were placed vertically at 90° relative to the photon-beam direction and a distance of 28 cm from the target. The other two HPGe detectors were positioned in a horizontal plane at 127° to the beam and at a distance of 32 cm from the target. Absorbers of 8 mm of Pb plus 3 mm of Cu and of 3 mm of Pb plus 3 mm of Cu were placed in front of the detectors at 90° and 127°, respectively, in the measurement at 7.9 MeV, whereas absorbers of 13 mm of Pb plus 3 mm of Cu and of 8 mm of Pb plus 3 mm of Cu were used for the detectors at 90° and 127°, respectively, in the measurement at 11.2 MeV. Spectra of scattered photons were measured for 145 and 51 h in the experiments at 7.9- and 11.2-MeV electron energy, respectively. To identify γ rays from ^{86}Kr, measurements with an empty steel container were carried out for comparison. Gamma-ray spectra of the empty container were measured for 55 and 45 h at electron energies of 7.9 and 11.2 MeV, respectively. Peaks observed in the spectrum measured with ^{86}Kr, but not observed in the spectrum of the empty container, were assigned to transitions in ^{86}Kr. Parts of the spectra including events measured with the two detectors placed at 127° relative to the beam at an electron energy of 11.2 MeV are shown in Fig. 1 for the steel container filled with ^{86}Kr and for the empty container.

The absolute photon flux at ELBE was determined from intensities and known integrated scattering cross sections of transitions in ^{11}B. For interpolation, the photon flux was calculated using a code [32] based on the approximation given in Ref. [33] and including a screening correction according to Ref. [34]. In addition, the flux was corrected for the attenuation by the beam hardener. This flux curve was adjusted to the experimental values obtained at the energies of levels in ^{11}B.

Measurements at various electron energies allowed us to estimate the influence of feeding on the integrated cross sections. Ratios of the quantities I_{s+f} obtained for levels in ^{86}Kr from the measurements at the two electron energies are shown in Fig. 2. The plotted ratios reveal that only levels below $E_x \approx 6$ MeV are influenced considerably by feeding. Transitions found in the measurement at $E_e^{\mathrm{kin}} = 7.9$ MeV are assumed to be ground-state transitions. Transitions additionally observed up to 7.9 MeV in the measurement at 11.2 MeV are consequently

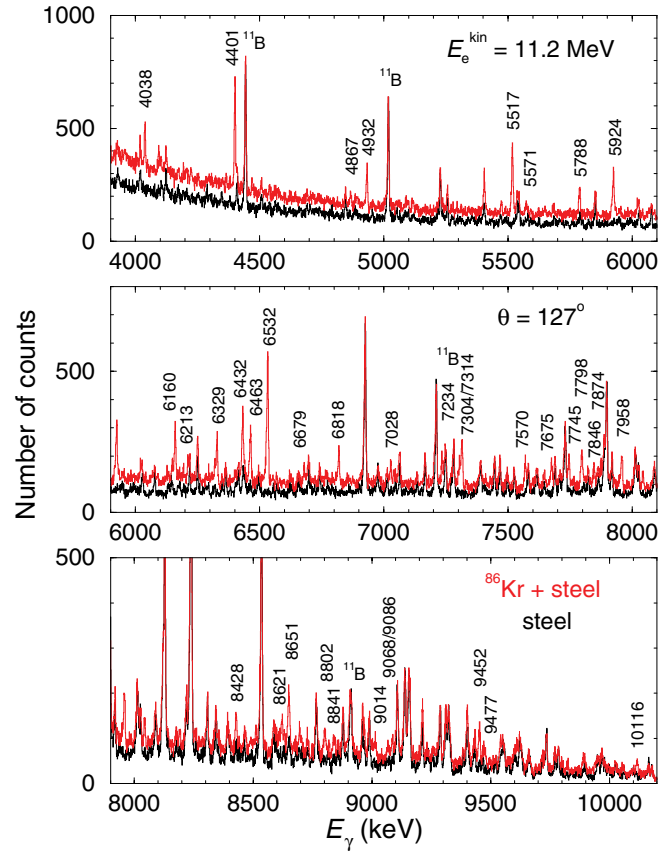

FIG. 1. (Color online) Parts of a spectrum of photons scattered from ^{86}Kr in a steel container combined with ^{11}B, measured during the irradiation with bremsstrahlung produced by electrons of an energy of $E_e^{\mathrm{kin}} = 11.2$ MeV. This spectrum is the sum of the spectra measured with the two detectors placed at 127° relative to the beam. Transitions assigned to ^{86}Kr are marked with their energies in keV. For comparison, the corresponding parts of a spectrum measured under the same conditions with an empty container are shown.

considered as inelastic transitions from high-lying to low-lying excited states. By comparing the respective spectra, these inelastic transitions were sorted out. The remaining ground-state transitions were used to derive the corresponding level energies which are listed in Table I together with spin assignments deduced from angular distributions of the ground-state transitions and integrated scattering cross sections. For states with $E_x < 5$ MeV, integrated scattering cross sections are not given because they may be influenced by feeding even in the experiment with 7.9-MeV electron energy.

E. Experiments with monoenergetic and linearly polarized γ radiation at HIγS

Monoenergetic photon beams are produced at HIγS by Compton backscattering of a high-intensity free-electron laser (FEL) beam from an intense electron beam in the Duke storage ring. Presently, the energy of the backward scattered photons can be tuned in a wide energy range, from about 1 to 100 MeV, by changing the energy of the electron beam and the FEL wavelength [24]. The polarization of the FEL photons, defined by the magnetic field of the undulators, is mostly preserved

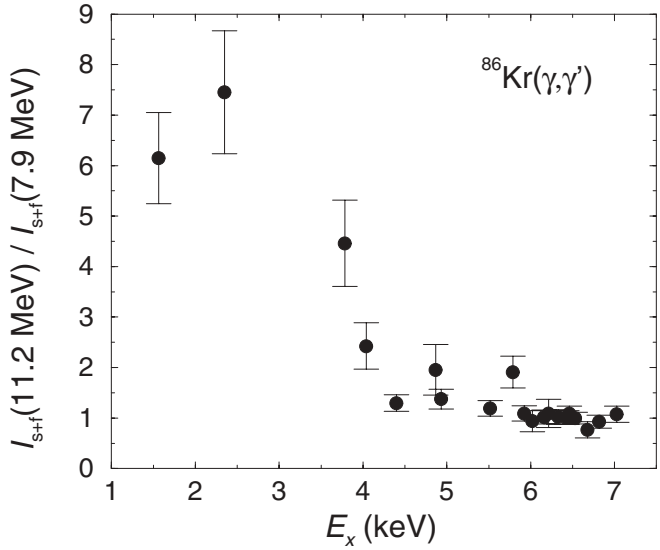

FIG. 2. Ratios of integrated cross sections I_{s+f} of transitions in ^{86}Kr obtained at electron energies of 7.9 and 11.2 MeV.

during the Compton backscattering due to a negligible recoil effect, leading to the production of intense photon beams with a degree of polarization of nearly 100%.

The measurements at HIγS were carried out at γ-ray energies of 4.7, 5.1, 5.6, 6.1, 6.5, 7.0, 7.5, 8.0, 8.4, 8.7, 9.0, and 9.3 MeV. The energy spread (full width at half maximum) of the beam was about 3% of the energy using a 30.5-cm-long lead collimator with a cylindrical hole of 1.9 cm in diameter positioned 60 m downstream from the collision point of the electrons with the FEL photons. The measuring time was about 7 h for each selected energy. The photon beam impinged onto the target with a flux of about 5×10^6 s^{-1} for the lowest energies up to 3×10^7 s^{-1} for the highest energies. Scattered photons were measured with two HPGe detectors taken from the detector setup at ELBE (see Sec. II D) without BGO shields. The detectors were placed at polar angles of 90° to the beam, one vertically on top of the beam tube and one horizontally downstream right of the beam tube at distances of 10 cm from the beam axis. Lead absorbers of 6 mm in thickness were placed in front of the detectors.

The type of radiation ($E1$ or $M1$) was deduced from a comparison of the intensities of the transitions measured at different azimuthal angles [26,36]. In the present setup, $E1$ radiation is detected preferentially in the vertical detector and $M1$ radiation in the horizontal detector. As an example, spectra measured at a beam energy of 6.5 MeV are shown in Fig. 3. The spectra allow a clear distinction between $E1$ and $M1$ radiation. Azimuthal asymmetries $A = (I_{\gamma H} - I_{\gamma V})/(I_{\gamma H} + I_{\gamma V})$ deduced from the intensities $I_{\gamma H}$ measured in the horizontal detector and $I_{\gamma V}$ measured in the vertical detector are given in Table I together with the resulting parities assigned to the emitting states. All the states listed in Table I have negative parity. Several peaks observed with the horizontal detector were assigned to $M1$ transitions in ^{56}Fe, which is a main component of the steel container. Some small peaks could not be uniquely assigned and it cannot be excluded that these

TABLE I. Levels assigned to ^{86}Kr.

E_x (keV)[a]	$\frac{I_\gamma(90°)}{I_\gamma(127°)}$ [b]	A[c]	J^π_x[d]	I_s (eV b)[e]
1564.8(1)	1.07(7)		2^+[f]	
2349.4(2)	1.08(9)		2^+[f]	
3782.7(4)	0.92(19)			
4038.5(3)	1.0(2)			
4400.7(1)	0.79(6)		1	
4867.4(6)	0.75(12)	−0.87(15)	$1^{(-)}$	
4932.4(2)	0.91(9)			
5517.5(2)	0.72(8)	−0.84(5)	1^-	154(9)
5571.0(12)	0.72(5)		1	20(6)
5788.2(3)	0.86(12)		(1)	56(5)
5924.1(4)	0.83(7)	−0.98(2)	1^-	129(8)
6160.0(2)	0.81(10)	−0.93(7)	1^-	149(10)
6213.1(18)	0.5(2)		1	49(9)
6328.6(3)	0.65(9)	−0.95(6)	1^-	117(8)
6431.9(2)	0.85(7)	−0.98(3)	1^-	199(11)
6462.9(3)	0.75(7)	−0.94(4)	1^-	166(10)
6531.7(2)	0.74(6)	−0.95(2)	1^-	454(23)
6678.6(5)	0.53(16)		1	57(6)
6818.3(4)	0.76(8)	−0.99(9)	1^-	138(9)
7028.1(4)	0.81(13)	−0.99(2)	1^-	103(13)
7234.3(4)	0.87(13)		(1)	119(15)
7304.2(5)	0.62(8)	−0.75(31)	1^-	95(11)
7314.3(3)	0.79(10)	−0.96(4)	1^-	260(30)
7569.6(4)	0.73(12)	−0.95(6)	1^-	156(20)
7675.3(4)	0.68(15)		1	105(16)
7745.4(4)	0.79(15)		1	220(31)
7797.5(4)	0.63(13)	−0.90(10)	1^-	211(30)
7846.2(5)	0.79(18)	−0.94(8)	1^-	107(16)
7873.8(7)	0.71(16)	−0.84(12)	1^-	89(14)
7958.0(4)	0.72(13)	−1.00(1)	1^-	219(29)
8428.2(4)	0.74(16)	−0.99(1)	1^-	216(32)
8621.2(8)	0.8(2)	−0.98(3)	1^-	148(25)
8650.8(3)	0.65(9)	−0.82(6)	1^-	336(42)
8802.0(6)	0.66(15)		1	246(48)
8841.1(8)	1.0(5)	−0.90(15)	1^-	214(54)
9013.9(6)	1.05(19)	−0.77(24)	1^-	172(24)
9067.6(10)	0.6(2)		1	84(17)
9085.6(8)	0.59(14)	−0.93(9)	1^-	118(19)
9452.3(5)	0.83(12)		1	265(40)
9477.4(18)	1.3(5)			157(30)
10115.6(8)	0.77(14)		1	233(31)

[a]Excitation energy. The uncertainty of this and the other quantities in the table is given in parentheses in units of the last digit. This energy value was deduced from the γ-ray energy measured at 127° including a recoil and Dopppler-shift correction.

[b]Ratio of the intensities measured at angles of 90° and 127°. The expected values for an elastic dipole transition (spin sequence 0–1–0) and for an elastic quadrupole transition (spin sequence 0–2–0) are 0.74 and 2.15, respectively.

[c]Azimuthal asymmetry $A = (I_{\gamma H} - I_{\gamma V})/(I_{\gamma H} + I_{\gamma V})$ of the intensities $I_{\gamma H}$ and $I_{\gamma V}$ measured with the detectors placed in the horizontal and vertical planes, respectively. A negative asymmetry indicates $E1$ radiation and a positive asymmetry indicates $M1/E2$ radiation.

[d]Spin and parity deduced from angular correlation and azimuthal asymmetry, respectively, of the ground-state transition.

[e]Energy-integrated scattering cross section. The value is an average over the values obtained at 90° and 127°. Below an excitation energy of 7.0 MeV the value was deduced from the measurement at 7.9 MeV electron energy; otherwise it is from the measurement at 11.2 MeV.

[f]Spin and parity taken from previous work [35].

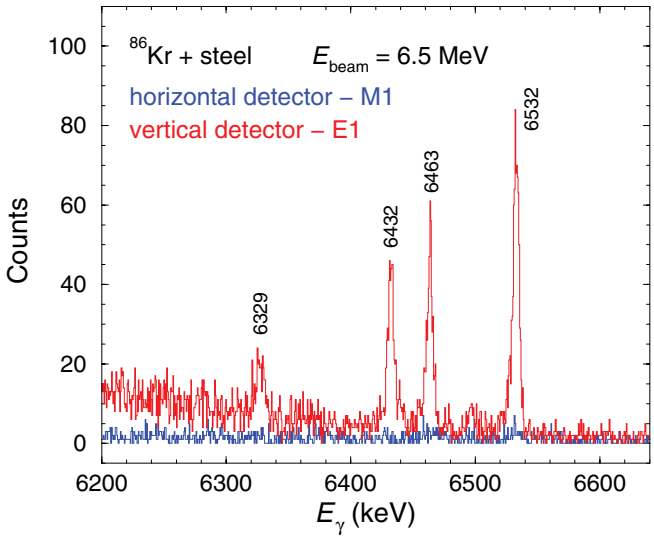

FIG. 3. (Color online) Parts of spectra of photons scattered from ^{86}Kr in a steel container, measured during the irradiation with quasimonoenergetic polarized γ rays of 6.5 MeV. The spectrum plotted in red was measured with the vertical detector and contains $E1$ radiation, whereas the spectrum plotted in blue was measured with the horizontal detector and contains $M1$ radiation. Transitions in ^{86}Kr are labeled with their energies in keV.

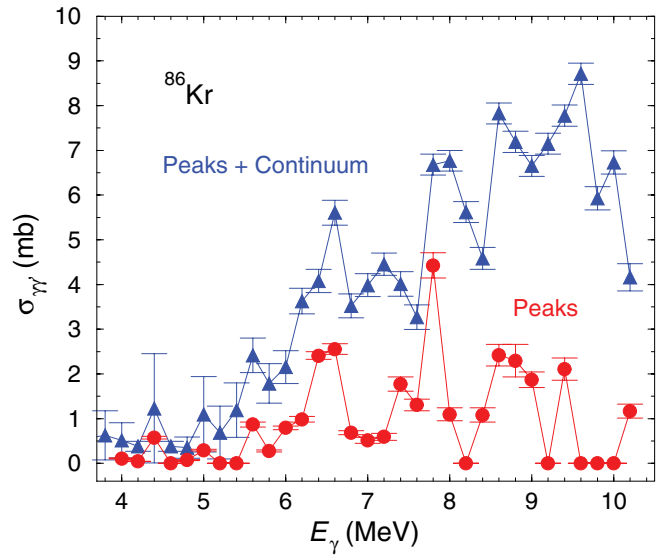

FIG. 4. (Color online) Scattering cross sections in ^{86}Kr, derived as $\sigma_{\gamma\gamma'} = \sum_\Delta I_s/\Delta$ for energy bins of $\Delta = 0.2$ MeV, not corrected for branching, as derived from the difference of the experimental spectrum and the atomic background ("Peaks + Continuum"; triangles) and from the resolved peaks only ("Peaks"; circles).

belong to $M1$ transitions in ^{86}Kr that are below the detection limit in the experiments at ELBE.

III. DETERMINATION OF THE DIPOLE-STRENGTH DISTRIBUTION

The determination of the dipole-strength distribution and the related photoabsorption cross section requires knowledge of the ground-state transitions and their branching ratios. As these cannot be derived directly from the measured spectra, we applied statistical methods described in the following.

First, the in-beam spectrum measured with the empty steel container at $E_e^{\rm kin} = 11.2$ MeV and containing signals of the two detectors at an equal observation angle was subtracted from the respective spectrum measured with the container filled with ^{86}Kr. Transitions following (n, γ) reactions in the HPGe detectors and in surrounding materials are negligibly small and thus did not require correction. To correct the spectra for detector response, spectra of monoenergetic γ rays were calculated in steps of 10 keV using GEANT4. Starting from the high-energy end of the experimental spectrum, the simulated spectra were subtracted sequentially.

The background radiation produced by atomic processes in the ^{86}Kr target was obtained from a GEANT4 simulation using the absolute photon flux deduced from the intensities of the transitions in ^{11}B. As found in previous studies [16–20, 37] the continuum in the spectrum of γ rays scattered from ^{86}Kr is considerably higher than the background due to atomic scattering. This continuum is formed by a large number of nonresolvable transitions with small intensities which are a consequence of the increasing nuclear level density at high energy in connection with the finite detector resolution (e.g., $\Delta E \approx 7$ keV at $E_\gamma \approx 9$ MeV).

The relevant intensity of the photons resonantly scattered from ^{86}Kr is obtained from a subtraction of the atomic background from the response-corrected experimental spectrum. The remaining intensity distribution includes the intensity contained in the resolved peaks as well as the intensity of the nuclear quasicontinuum. The scattering cross sections $\sigma_{\gamma\gamma'}$ derived for energy bins of 0.2 MeV from the full intensity distribution are shown in Fig. 4. These values are compared with those derived from the integrated scattering cross sections of the resolved transitions given in Table I. One sees that the two curves have similar structures caused by the prominent peaks. However, the curve including also the continuum part of the spectrum contains altogether a strength that is by a factor of about 5 greater than the strength of the resolved peaks only.

The full intensity distribution (resolved peaks and continuum) and the corresponding scattering cross sections shown in Fig. 4 contain (elastic) ground-state transitions and, in addition, branching transitions to lower-lying excited states (inelastic transitions) as well as subsequent transitions from those states to even lower states or to the ground state (cascade transitions). The different types of transitions cannot be clearly distinguished. However, for the determination of the photoabsorption cross section the intensities of the ground-state transitions are needed. Therefore, contributions of inelastic and cascade transitions have to be subtracted from the spectra. To correct the intensity distributions we performed simulations of γ-ray cascades from levels with $J = 0, 1, 2$ excited in the whole energy range up to the neutron-separation energy. The Monte Carlo code used is described in Ref. [38]. It works analogously to the code DICEBOX developed for γ-ray cascades following neutron capture [39] but in addition it includes the excitation from the ground state as a first step. In the present simulations, 1000 nuclear realizations, each starting with an excitation from the ground state, were

created with level densities derived from experiments [40]. We applied the statistical methods also for the low-energy part of the level scheme instead of using experimentally known low-lying levels in ^{86}Kr because this would require knowledge of the partial decay widths of all transitions populating these fixed levels. Fluctuations of the nearest-neighbor spacings were taken into account according to the Wigner distribution (see, e.g., Ref. [41]). The partial widths of the transitions to low-lying levels were assigned using *a priori* known strength functions for $E1$, $M1$, and $E2$ transitions. Fluctuations of the partial widths were treated by applying the Porter-Thomas distribution [42].

In the calculations, parameters of the back-shifted Fermi-gas (BSFG) model obtained from fits to experimental level densities [40], $a = 9.83(14)$ MeV^{-1} and $E_1 = 0.97(6)$ MeV, were used. In the individual nuclear realizations, the values of a and E_1 were varied within their uncertainties. As usual in the BSFG model, we assumed equal level densities for states with positive and negative parities of the same spin [40]. This assumption has been justified by the good agreement of level densities predicted by the BSFG model with experimental level densities of 1^+ states in the energy range from 5 to 10 MeV obtained from the ^{90}Zr(^{3}He, t)^{90}Nb reaction [43] and with experimental level densities of 2^+ and 2^- states in ^{90}Zr studied in the ^{90}Zr(e, e') and ^{90}Zr(p, p') reactions [44]. The extended analysis of the ^{90}Zr(^{3}He, t)^{90}Nb reaction in Ref. [44] indicates however fluctuations of the level density of 1^+ states in ^{90}Nb around the predictions of the BSFG model.

For the $E1$, $M1$, and $E2$ photon strength functions Lorentz parametrizations [1] were used. The parameters of the Lorentz curve for the $E1$ strength were determined according to the prescription given in Ref. [7], resulting in $E_0 = 17.1$ MeV and $\Gamma = 4.7$ MeV at zero deformation. The integral over this curve is consistent with the Thomas-Reiche-Kuhn (TRK) sum rule $\frac{\pi}{2}\sigma_0\Gamma = 60NZ/A$ MeV mb [45]. The parameters for the $M1$ and $E2$ strengths were taken from global parametrizations of $M1$ spin-flip resonances and $E2$ isoscalar resonances, respectively [2].

Spectra of γ-ray cascades were generated for groups of levels in 100-keV bins in each of the 1000 nuclear realizations. For illustration, the distributions resulting from 10 individual nuclear realizations populating levels in a 100-keV bin around 9 MeV are shown in Fig. 5. The levels were created randomly starting from the ground state, where however the strength function and level density are small. In contrast, starting with the known first excited state at 1.565 MeV would cause a gap in the spectra between $E_x = 1.565$ MeV and the considered excitation energy E_x. A spectrum simulated for a given energy bin is comparable to a spectrum measured using monoenergetic γ rays of this energy. For the present case, this comparison is however difficult because of the contribution of the steel container to the measured spectrum.

Starting from the high-energy end of the experimental spectrum, which contains ground-state transitions only, the simulated intensities of the ground-state transitions were adjusted to the experimental ones in the considered bin and the intensity distribution of the branching transitions was subtracted from the experimental spectrum. Applying this procedure step-by-step for each energy bin moving toward

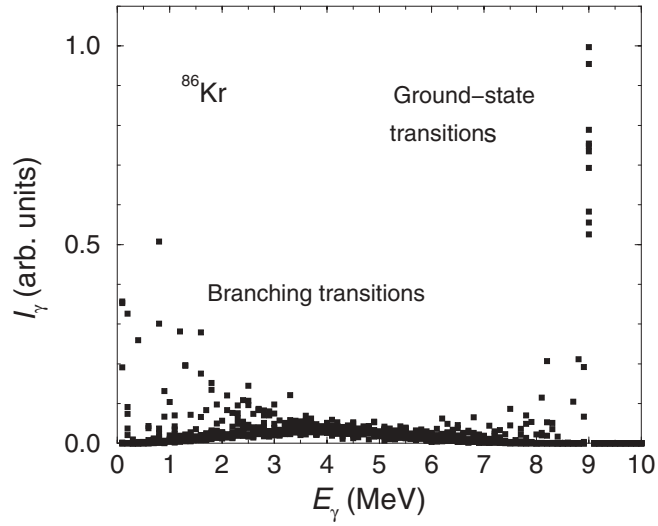

FIG. 5. Simulated intensity distribution of transitions depopulating levels in a 100-keV bin around 9 MeV in ^{86}Kr. The squares depict the intensities obtained from 10 individual nuclear realizations.

the low-energy end of the spectrum one obtains the intensity distribution of the ground-state transitions. Simultaneously, the branching ratios b_0^Δ of the ground-state transitions are deduced for each energy bin Δ. In an individual nuclear realization, the branching ratio b_0^Δ is calculated as the ratio of the sum of the intensities of the ground-state transitions from all levels in Δ to the total intensity of all transitions depopulating those levels to any low-lying levels including the ground state [16,18]. The absorption cross section for a bin is obtained by dividing the summed intensities in a bin of the experimental intensity distribution of the ground-state transitions by the corresponding branching ratio as $\sigma_\gamma^\Delta = \sigma_{\gamma\gamma'}^\Delta / b_0^\Delta$. Finally, the absorption cross sections of each bin were obtained by averaging over the values of the 1000 nuclear realizations. For the uncertainty of the absorption cross section a 1σ deviation from the mean has been taken.

The individual branching ratios of 10 nuclear realizations are shown in Fig. 6. The mean branching ratio of the 1000 realizations decreases from about 90% for low-lying states, where only few possibilities for the deexcitation to lower-lying states exist, to about 40% at the neutron-separation energy $S_n = 9.9$ MeV. Toward low energy the uncertainty of b_0^Δ increases due to level-spacing fluctuations and the decreasing level density. The large fluctuations below about 6 MeV make these values useless. Note that the mean branching ratio is not representative for transitions with large intensities such as the resolved transitions given in Table I. It turns out from the cascade simulations that the branching ratios of ground-state transitions deexciting states with integrated scattering cross sections like the ones given in Table I are in the order of $b_0 \approx 85\%$ to 99% which is in agreement with experimental findings. This behavior was discussed in our study of the neighboring $N = 50$ isotone ^{88}Sr [18]. In measurements with monoenergetic γ rays, the branching ratios can be deduced directly from the experimental intensity distributions of the elastic and inelastic transitions and do not need to be simulated. This is however difficult in the present case because of the

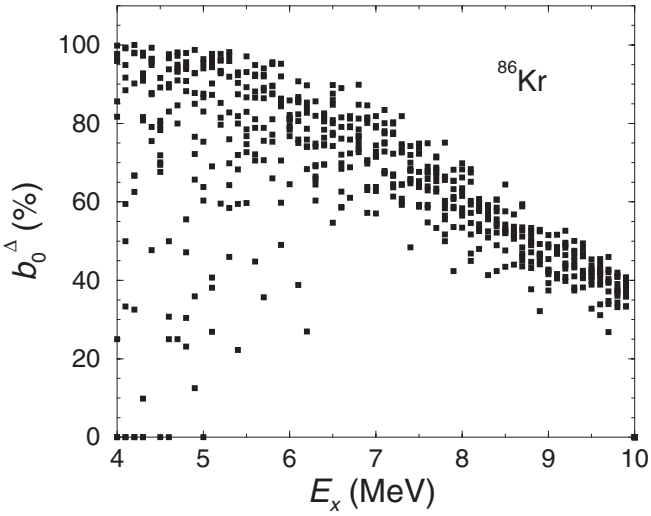

FIG. 6. Branching ratios of ground-state transitions as obtained from simulations of γ-ray cascades for ^{86}Kr. The squares represent the values of 10 individual nuclear realizations.

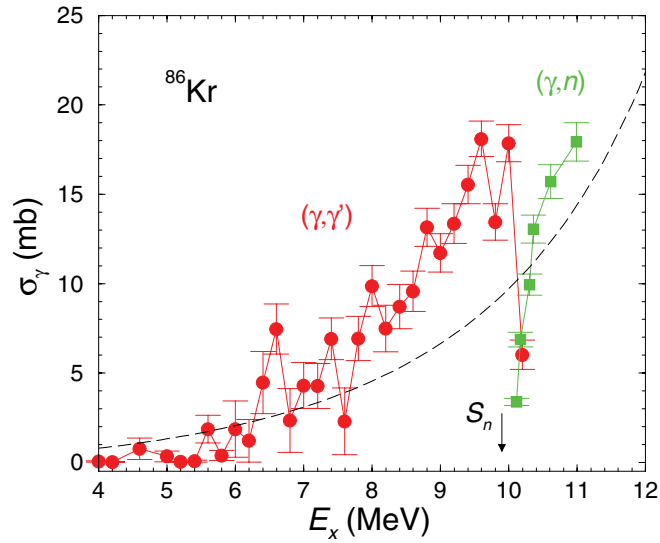

FIG. 7. (Color online) Photoabsorption cross section deduced from the present ^{86}Kr(γ, γ') experiments at ELBE after correction for branching transitions (red circles) in comparison with ^{86}Kr(γ, n) cross sections obtained by using monoenergetic γ rays at HIγS (green squares) [48]. The black dashed line is a Lorentz curve with parameters given in the text.

contributions of the radiation from the steel container. We deduced branching ratios from spectra measured at HIγS for the cases of ^{98}Mo [46] and ^{136}Ba [29]. The analysis of these spectra was analogous to the one just described in connection with the experiments at ELBE; i.e., the spectra were corrected for detector response, the atomic background was subtracted, and the intensity in the continuum was also considered. This procedure is illustrated in Ref. [29]. The experimental branching ratios deduced in this way from spectra measured at HIγS for ^{98}Mo [46] and ^{136}Ba [29] are in good agreement with the ones obtained from the cascade simulations. This agreement proves the reliability of the simulations of γ-ray cascades as used in the present analysis.

In a recently published study of ^{142}Nd at HIγS [47] branching ratios are shown that were deduced from resolved peaks and do not include strength in the continuum (cf. Fig. 1 of Ref. [47]), in contrast to the just mentioned procedure applied in Refs. [29,46]. That causes large branching ratios of up to 100% at energies up to 6 MeV, as usual for strong transitions (cf. values just given and Ref. [18]), and produces pronounced kinks in the curve of b_0 versus E_γ instead of a smooth behavior. As pointed out in our investigation of ^{88}Sr [18], these strong transitions do not obey statistical characteristics such as Porter-Thomas distributions. In Ref. [47] the b_0 values deduced from transitions in ^{142}Nd were compared with the ones obtained from cascade simulations with DICEBOX using various assumptions for the input strength functions. A reproduction of the discontinuous behavior of the experimental b_0 was achieved with the very specific assumption of a small soft pole of 0.6-mb maximum cross section at $E_\gamma = 1.0$ MeV, which was applied to states in a narrow energy window from 4.9 to 6.3 MeV. This energy window is below the PDR region in ^{142}Nd and does not affect the absorption cross section above 6 MeV. Indeed, the absorption cross section of ^{142}Nd presented in Ref. [47] resembles the one deduced for ^{136}Ba from our experiments at ELBE and HIγS [29] in magnitude and location, although the double-hump structure seen in ^{142}Nd is less pronounced in ^{136}Ba. This similarity confirms our earlier finding that the cross section corrected for branching on the basis of cascade simulations is not very sensitive to variations of the shape of the input strength function, which we studied for the case of ^{90}Zr [19].

The photoabsorption cross sections derived from the present experiments for ^{86}Kr are shown in Fig. 7. In addition, the values obtained from a ^{86}Kr(γ, n) experiment at the HIγS facility [48] are shown. The total photoabsorption cross section was deduced by combining the present (γ, γ') data with the (γ, n) data of Ref. [48]. The values averaged over energy bins of 500 keV are shown in Fig. 8.

IV. DISCUSSION

The experimental absorption cross section shown in Fig. 8 has a peak at about 6.5 MeV and a resonance-like structure in the energy range from about 7 to 11 MeV. Such a structure has also been found in the neighboring $N = 50$ isotones and is shown for ^{88}Sr [18], ^{90}Zr [19], and ^{92}Mo [17] in Fig. 9. This structure strongly resembles the PDR observed in other neutron-rich nuclei, which is explained as a vibration of the excessive neutrons against the symmetric $N = Z$ system and is expected to correlate with the ratio N/Z [12–14].

To examine the behavior of the strength with varying N/Z we deduced the sums of the measured absorption cross sections weighted with the corresponding energy bins in the energy range from 6 to 10 MeV for the even-even isotones. The resulting quantities $\sum_{6\,\mathrm{MeV}}^{10\,\mathrm{MeV}} \sigma_i \Delta E_i$ are shown in Fig. 10. The ratio N/Z varies from 1.39 for ^{86}Kr to 1.19 for ^{92}Mo. There is no clear tendency discernible for this series of isotones. However, the closed proton subshells, $\pi(1p_{3/2})$ at $Z = 38$ (^{88}Sr)

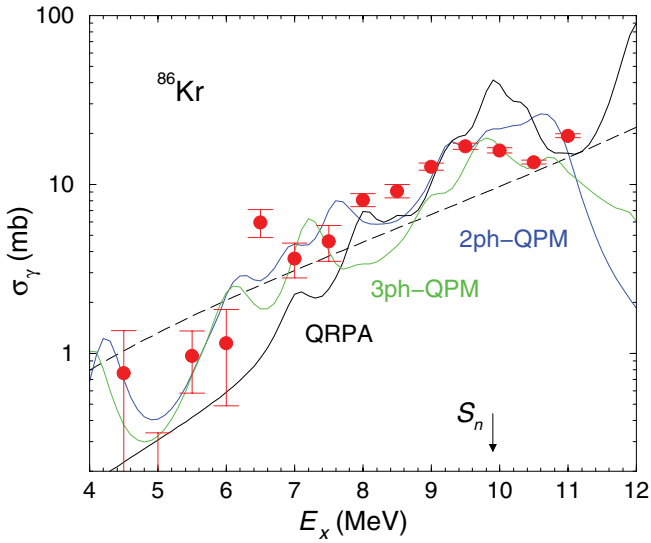

FIG. 8. (Color online) Total photoabsorption cross section of ^{86}Kr including (γ, γ') and (γ, n) data (red circles) compared with results of QRPA (black line) and two-phonon QPM (blue line) and three-phonon QPM (green line) calculations. The QRPA and QPM solutions were folded with Lorentz curves of 0.5 MeV width. The black dashed line is a Lorentz curve with parameters given in Sec. III.

and in addition $\pi(1p_{1/2})$ at $Z = 40$ (^{90}Zr), seem to cause larger strength. In fact, there are intense isolated resonances in the absorption cross sections of these nuclides [18,19]. For the chain of stable $N = 82$ isotones with ratios N/Z varying from 1.52 for ^{136}Xe to 1.32 for ^{144}Sm an increase of the strength summed up to an energy of 8 MeV with increasing N/Z was observed [49,50]. This feature was attributed at least in part to the fact that there is strength missing because of the sensitivity limit of the experiments and it tends to vanish when applying a

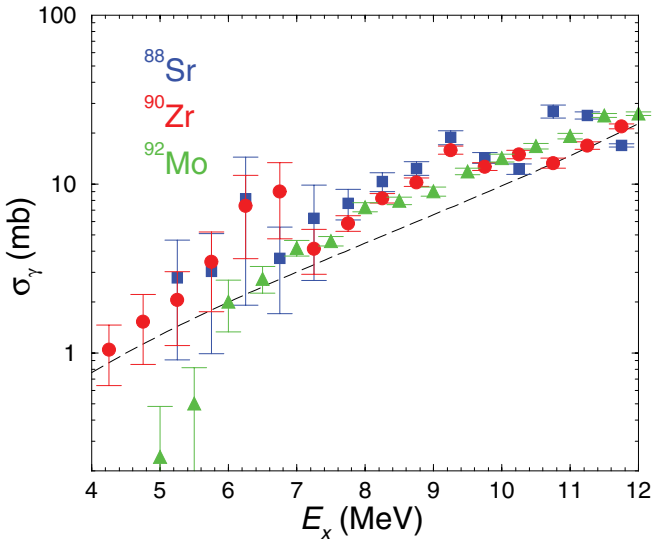

FIG. 9. (Color online) Total photoabsorption cross sections of ^{88}Sr (blue squares), and ^{90}Zr (red circles), ^{92}Mo (green triangles) and a Lorentz curve (black dashed line) adjusted to ^{88}Sr(γ, n) cross sections. The data were taken from Refs. [17–19].

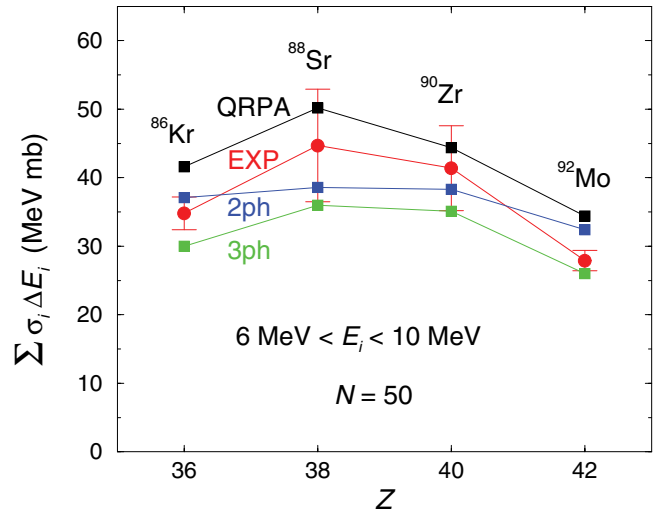

FIG. 10. (Color online) Energy-weighted sums of photoabsorption cross sections for the excitation energy region from 6 to 10 MeV for the even-even stable $N = 50$ isotones. The data for ^{88}Sr, ^{90}Zr, and ^{92}Mo were taken from Refs. [17–19].

corresponding correction [49,50]. Experiments on the $N = 82$ nuclides ^{139}La at ELBE [37] and ^{138}Ba at HIγS [51] as well as on the $N = 80$ neighbor ^{136}Ba at ELBE and HIγS [29] take into account the strength in the quasicontinuum and the branching ratios of the ground-state transitions. However, there is information on further $N = 82$ isotones needed for a systematic investigation of the PDR strength in that mass region.

For the interpretation of the present data for ^{86}Kr in connection with the findings for the $N = 50$ isotones just mentioned we use a self-consistent theoretical approach based on the density-functional theory [52] and the QPM [53] as described in detail in Ref. [13]. The results for ^{86}Kr calculated using the QRPA and the three-phonon QPM [54] are compared with the experimental results in Fig. 8 and are discussed in the following.

In the case of $N = 50$ isotones the neutron number is fixed and the proton number changes, which affects the thickness δr of the neutron skin as well. This can be seen in ground-state proton- and neutron-density distributions and in (relative) differences of proton and neutron root-mean-square (rms) radii,

$$\delta r = \sqrt{\langle r^2 \rangle_n} - \sqrt{\langle r^2 \rangle_p}, \tag{3}$$

defining the thickness of the neutron skin [19]. The tendencies of δr and of the total $B(E1)$ strength up to 9 MeV with varying N/Z in the considered $N = 50$ isotones are illustrated by results of Hartree-Fock-Bogoliubov calculations shown in Figs. 11 and 12, respectively.

The QRPA calculations of low-energy dipole states with excitation energies up to $E_x = 22$ MeV in ^{86}Kr, ^{88}Sr, ^{90}Zr, and ^{92}Mo nuclei show as a common feature a sequence of almost pure neutron 1^- states located in the energy range $E_x <$ 9 MeV, which is in agreement with our previous results for ^{88}Sr and ^{90}Zr presented in Ref. [19]. These states correspond to excitations of least bound neutrons from a valence orbit

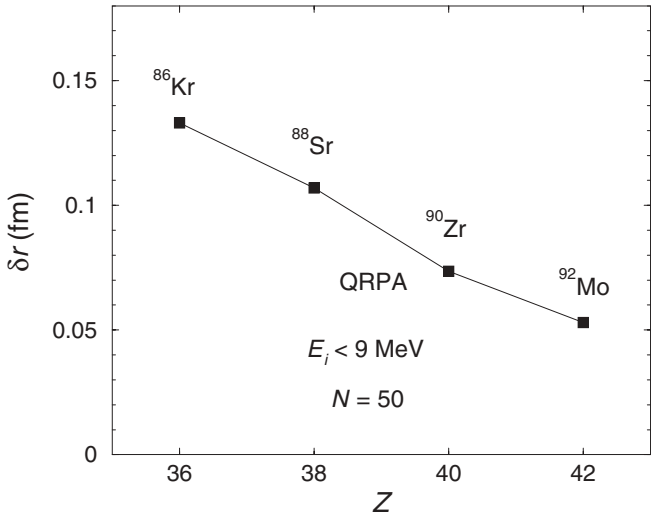

FIG. 11. Calculated differences of neutron and proton rms radii defining the neutron skin thickness for $N = 50$ isotones.

to a higher orbit, such as $0f_{5/2} \rightarrow 1d_{5/2}$, $1p_{1/2} \rightarrow 2s_{1/2}$, $1p_{3/2} \rightarrow 1d_{5/2}$, and $0g_{9/2} \rightarrow 0h_{11/2}$, but with only a minor proton contribution of less than 1% and they are related to neutron skin oscillations and the PDR. The structure of these states is dominated by one two-quasiparticle (2qp) neutron component, showing that these excitations are of noncollective character. Similar results were found in $Z = 50$ and $N = 82$ nuclei [13,55]. Insight into the properties of the excitations is gained from an inspection of transition densities calculated according to the procedure described in Ref. [14] and shown in Fig. 13. The transition densities of the 1^- states with $E_x <$ 9 MeV display clear signals of a PDR mode, in agreement with our previous studies [13,19]. Namely, we observe in-phase oscillations of protons and neutrons in the nuclear interior, whereas at the surface only neutrons contribute. These features are characteristic for dipole skin vibrations [13]. QRPA calculations of the sum strength $\sum_{0\ \mathrm{MeV}}^{9\ \mathrm{MeV}} B(E1)\uparrow$ related to

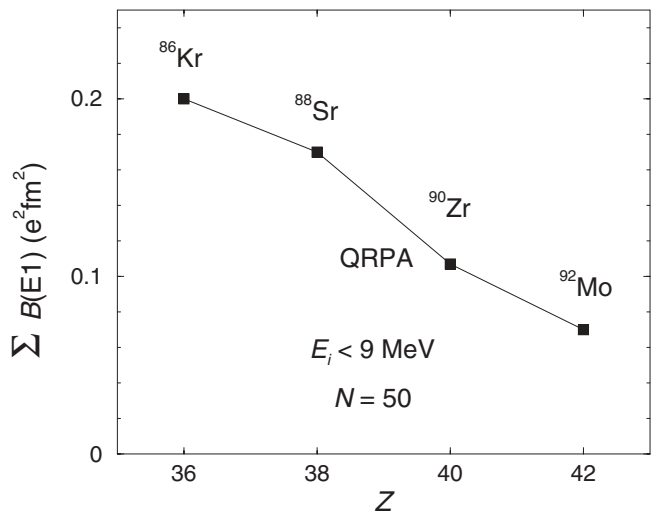

FIG. 12. Total $B(E1)$ strength up to 9 MeV obtained from QRPA calculations for $N = 50$ isotones.

the PDR in $N = 50$ isotones are presented in Fig. 12. As can be seen, the total PDR strength decreases with increasing proton number, i.e., with decreasing N/Z. Finally, we note that the results are in agreement with the established connection between the calculated total PDR strength and the nuclear skin thickness defined in Eq. (3).

The analysis of the evolution of dipole transition densities with increasing excitation energy allows us to distinguish between the PDR and other types of dipole excitations. In this respect, the states in the energy region of $9 < E_x < 10$ MeV carry a signature different from the PDR. The protons and neutrons start to move out of phase, being compatible with the low-energy part of the GDR. A strong argument in this direction is that the observed amount of dipole strength located in the region $9 < E_x < 10$ MeV cannot be directly connected to N/Z ratios and corresponding skins, as can be done for the dipole strength below 9 MeV. A further increase of energy in the range of $10 < E_x < 11$ MeV leads to dynamic processes of collective excitations of different neutron and proton subshells of the nuclear interior, which in some cases could be in-phase as shown in Fig. 13. The presence of in-phase collective dipole excitations closely above the neutron threshold is also observed in collective model approaches [56], in which attempts are made to relate that to the PDR spectral component. However, it is clear that such more or less collective excitations including a considerable contribution of inner-shell neutrons and protons should not be interpreted in the same way as the genuine PDR mode explained by neutron skin oscillations. At $E_x = 11$ to 22 MeV a strong isovector oscillation corresponding to the excitation of the GDR is found.

The comparison of QRPA with two-phonon (2ph) and three-phonon (3ph) QPM calculations which include even- and odd-parity states with spins $1 \geqslant J \leqslant 5$ and excitation energies $E_x < 11$ MeV indicates that for the PDR region the coupling of PDR- and GDR-QRPA phonons and multiphonon states is very important. This coupling causes a fragmentation of the strength that results in a smoothing of the usual QRPA fluctuations and a shift of $E1$ strength toward lower energy, as is well visible in Fig. 8. Consequently, the QPM calculations predict about two times greater total $E1$ strength than the QRPA calculations do in the energy range $0 < E_x < 9$ MeV and are in better agreement with the experimental findings. The enhanced strength in ^{86}Kr observed in the region above $E_x =$ 6 MeV is related to the PDR as identified from the structure of the involved 1^- states. The contribution of the GDR dynamics becomes significant at energies $E_x > 9$ MeV where a coupling among PDR, GDR, and multiphonon states reflects the properties of the dipole excitations at higher energies. With increasing excitation energy toward the GDR region, the sum $B(E1)$ strengths obtained from QRPA and QPM calculations are of comparable amount, which suggests the predominance of one-phonon excitations of collective GDR type.

The experimental total energy-integrated cross sections in the region of $E_x = 6$ to 10 MeV, $\sum_{6\ \mathrm{MeV}}^{10\ \mathrm{MeV}} \sigma_i \Delta E_i$, are compared with sums over energy-integrated cross sections obtained according to $\sum_{6\ \mathrm{MeV}}^{10\ \mathrm{MeV}} I_s/(\mathrm{MeV\ mb}) = \sum_{6\ \mathrm{MeV}}^{10\ \mathrm{MeV}} [4.03 E_x/\mathrm{MeV}\ B(E1)\uparrow/(e^2\mathrm{fm}^2)]$ [5] from the QRPA and QPM calculations for the considered $N = 50$ isotones in Fig. 10. This comparison shows that the $\sum I_s$ deduced from the one-, two-, and

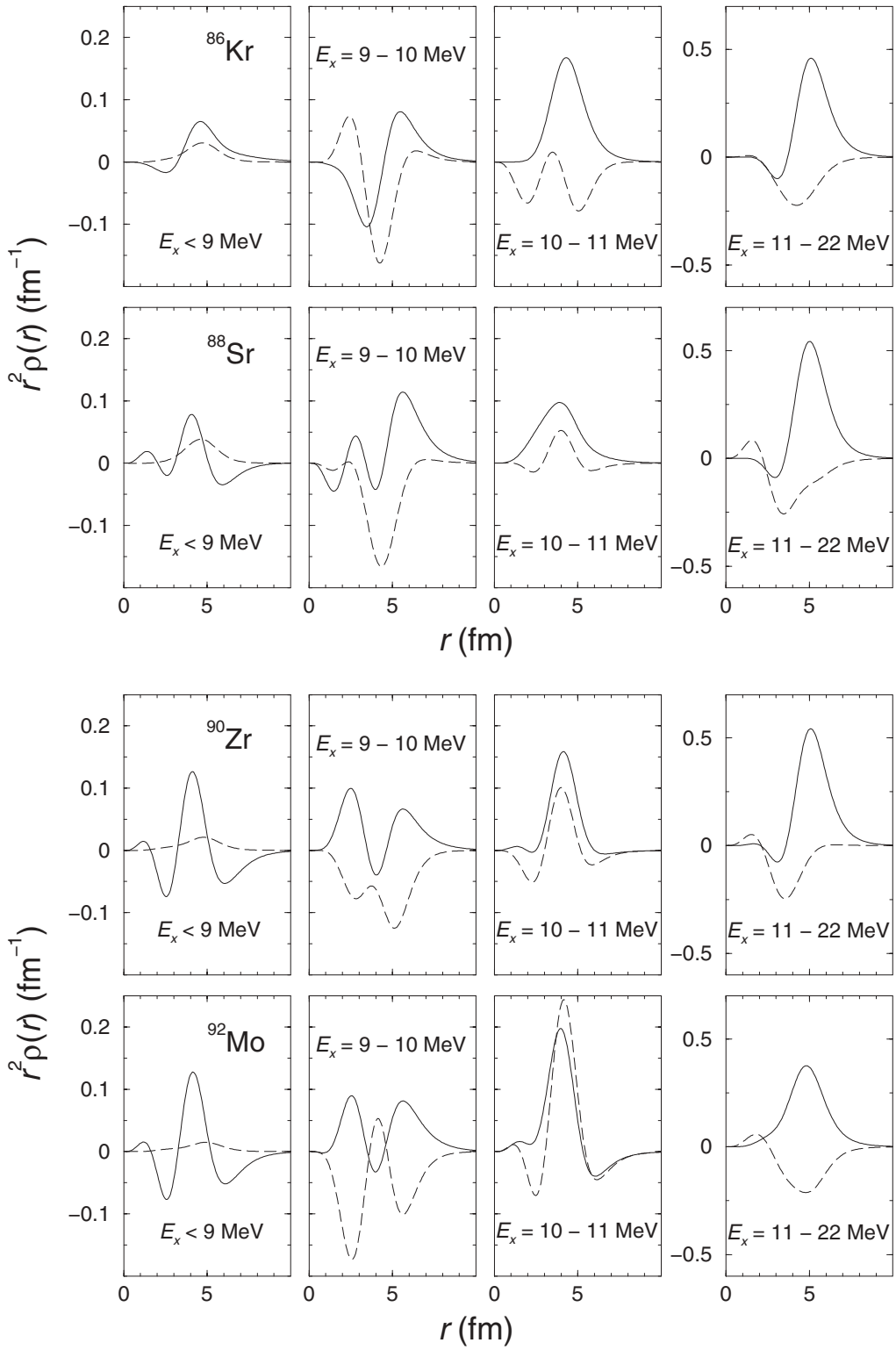

FIG. 13. Transition densities of neutrons (solid lines) and protons (dashed lines) in $N = 50$ isotones.

three-phonon calculations of 1^- states with energies up to $E_x = 10$ MeV reproduce the experimental values and the systematic behavior of the total $E1$ strength with varying N. The comparison demonstrates that the relative differences between the $E1$ strengths calculated within QRPA and QPM for the energy region above $E_x = 9$ MeV decrease with the increase of the excitation energy toward the GDR, which is expected because of the weak dependence of the GDR strength on the N/Z ratios in the $N = 50$ isotones. Hence, the tendency shown in Fig. 12 for the QRPA calculations is washed out. Similar results were found for tin nuclei [13]. In general, both the QRPA and QPM calculations are found to be

reliable for the description of the experimental values of the total photoabsorption cross sections in $N = 50$ isotones and their isotonic dependence at high energy.

V. SUMMARY

The dipole-strength distribution in ^{86}Kr up to the neutron-separation energy has been studied in photon-scattering experiments at the ELBE accelerator using various electron energies. Ground-state transitions were identified by comparing the transitions observed at different electron energies. We identified 39 levels. Spin $J = 1$ was deduced from angular correlations of ground-state transitions for 33 levels. The parities of 22 states were determined from azimuthal asymmetries of intensities measured in an experiment with monoenergetic and polarized γ radiation at the HIγS facility.

The intensity distribution obtained from the measured spectra after a correction for detector response and a subtraction of atomic background in the target contains a continuum part in addition to the resolved peaks. It turns out that the dipole strength in the resolved peaks amounts to about 16% of the total dipole strength whereas the continuum contains about 84%.

An assignment of inelastic transitions to particular levels and, thus, the determination of branching ratios was in general not possible. To get information about the intensities of inelastic transitions to low-lying levels we have applied statistical methods. By means of simulations of γ-ray cascades intensities of branching transitions were estimated and subtracted from the experimental intensity distribution and the intensities of ground-state transitions could be corrected on average for their branching ratios.

A comparison of the photoabsorption cross section obtained in this way from the present (γ, γ') experiments with (γ, n) data shows a smooth connection of the data of the two different experiments and gives new information about the extension of the dipole-strength function toward energies around and below the threshold of the (γ, n) reaction. In comparison with a straightforward approximation of the GDR by a Lorentz curve one observes extra $E1$ strength in the energy range from 6 to 11 MeV which is mainly concentrated in strong peaks.

QPM calculations for ^{86}Kr predict low-energy dipole strength in the energy region from 6 to 10 MeV. As the theoretical analysis shows, the states at about 6 to 7.5 MeV have a special character. Their structure is dominated by neutron components and their transition strengths are directly related to the size of a neutron skin. Their generic character is further confirmed by the shape and structure of the related transition densities, showing that these PDR modes are clearly distinguishable from the GDR. The dipole states, seen as a rather fragmented ensemble at $E_x > 7.5$ MeV, mix strongly with the low-energy tail of the GDR starting to appear in the same region. The complicated structure of these states and the high level densities imposes considerable difficulties for a reliable description of the fragmentation pattern.

The present analysis shows that standard strength functions currently used for the calculation of cross sections in codes based on statistical reaction models do not describe the dipole-strength distribution below the (γ, n) threshold correctly and need to be improved by taking into account the observed enhanced strength. Consequences of the use of experimental strength functions as an input for calculations with the statistical reaction model in comparison with standard input strength functions based on Lorentz curves were investigated by means of calculations with the TALYS code [57] for the nuclides $^{92-100}$Mo, ^{88}Sr, ^{90}Zr, and ^{139}La [58]. It turned out that very pronounced PDR strength, for example that in ^{139}La, causes an increase of the (n, γ) cross section and the astrophysical reaction rate.

ACKNOWLEDGMENTS

We thank the staff of the ELBE accelerator and the staff of the Duke storage ring and FEL for their cooperation during the experiments. We also thank A. Hartmann for technical assistance and Drs. E. Birgersson, M. Erhard, K. Kosev, A. Matic, and C. Nair for their help during the experiments. We gratefully acknowledge the support of Dr. F. Käppeler during the preparation of the high-pressure gas container.

[1] P. Axel, Phys. Rev. **126**, 671 (1962).
[2] R. Capote *et al.*, Nucl. Data Sheets **110**, 3107 (2009).
[3] S. G. Kadmenskii, V. P. Markushev, and V. I. Furman, Sov. J. Nucl. Phys. **37**, 165 (1983) [Yad. Fiz. **37**, 277 (1983)].
[4] J. Kopecky and M. Uhl, Phys. Rev. C **41**, 1941 (1990).
[5] A. Bohr and B. R. Mottelson, *Nuclear Structure*, Vol. II (Benjamin, Reading, MA, 1975).
[6] J. M. Eisenberg and W. Greiner, *Nuclear Theory*, Vol. I (North-Holland, Amsterdam, 1975), Chaps. 10 and 11.
[7] A. R. Junghans, G. Rusev, R. Schwengner, A. Wagner, and E. Grosse, Phys. Lett. B **670**, 200 (2008).
[8] M. Danos and W. Greiner, Phys. Lett. **8**, 113 (1964).
[9] M. G. Huber, M. Danos, H. J. Weber, and W. Greiner, Phys. Rev. **155**, 1073 (1967).
[10] G. A. Bartholomew, E. D. Earle, A. J. Ferguson, J. W. Knowles, and M. A. Lone, Adv. Nucl. Phys. **7**, 229 (1973).
[11] N. Tsoneva, H. Lenske, and Ch. Stoyanov, Phys. Lett. B **586**, 213 (2004).
[12] N. Tsoneva and H. Lenske, Prog. Part. Nucl. Phys. **59**, 317 (2007).
[13] N. Tsoneva and H. Lenske, J. Phys. G **35**, 014047 (2008).
[14] N. Tsoneva and H. Lenske, Phys. Rev. C **77**, 024321 (2008).
[15] J. Endres *et al.*, Phys. Rev. Lett. **105**, 212503 (2010).
[16] G. Rusev *et al.*, Phys. Rev. C **77**, 064321 (2008).
[17] G. Rusev *et al.*, Phys. Rev. C **79**, 061302(R) (2009).
[18] R. Schwengner *et al.*, Phys. Rev. C **76**, 034321 (2007).
[19] R. Schwengner *et al.*, Phys. Rev. C **78**, 064314 (2008).
[20] N. Benouaret *et al.*, Phys. Rev. C **79**, 014303 (2009).
[21] R. Schwengner *et al.*, Nucl. Instrum. Methods A **555**, 211 (2005).
[22] F. Gabriel, P. Gippner, E. Grosse, D. Janssen, P. Michel, H. Prade, A. Schamlott, W. Seidel, A. Wolf, and R. Wünsch, Nucl. Instrum. Methods B **161**, 1143 (2000).

[23] J. Teichert, A. Büchner, P. Evtushenko, F. Gabriel, U. Lehnert, P. Michel, and J. Voigtländer, Nucl. Instrum. Methods A **507**, 354 (2003).
[24] H. R. Weller, M. W. Ahmed, H. Gao, W. Tornow, Y. K. Wu, M. Gai, and R. Miskimen, Prog. Part. Nucl. Phys. **62**, 257 (2009).
[25] F. Ajzenberg-Selove, Nucl. Phys. A **506**, 1 (1990).
[26] G. Rusev, A. P. Tonchev, R. Schwengner, C. Sun, W. Tornow, and Y. K. Wu, Phys. Rev. C **79**, 047601 (2009).
[27] G. Rupp, D. Petrich, F. Käppeler, J. Kaltenbaek, B. Leugers, and R. Reifarth, Nucl. Instrum. Methods A **608**, 152 (2009).
[28] S. Agostinelli *et al.*, Nucl. Instrum. Methods A **506**, 250 (2003).
[29] R. Massarczyk *et al.*, Phys. Rev. C **86**, 014319 (2012).
[30] E. Trompler, Diploma thesis, Technische Universität Dresden, 2009, http://www.hzdr.de/publications/013364/13364.pdf.
[31] S. Carson *et al.*, Nucl. Instrum. Method A **618**, 190 (2010).
[32] E. Haug, Rad. Phys. Chem. **77**, 207 (2008).
[33] G. Roche, C. Ducos, and J. Proriol, Phys. Rev. A **5**, 2403 (1972).
[34] F. Salvat, J. D. Martinez, R. Mayol, and J. Parellada, Phys. Rev. A **36**, 467 (1987).
[35] B. Singh, Nucl. Data Sheets **94**, 1 (2001).
[36] N. Pietralla *et al.*, Phys. Rev. Lett. **88**, 012502 (2002).
[37] A. Makinaga *et al.*, Phys. Rev. C **82**, 024314 (2010).
[38] G. Rusev, Dissertation, Technische Universität Dresden, 2007, http://www.hzdr.de/publications/010008/10008.pdf.
[39] F. Bečvář, Nucl. Instrum. Methods A **417**, 434 (1998).
[40] T. von Egidy and D. Bucurescu, Phys. Rev. C **80**, 054310 (2009).
[41] T. A. Brody, J. Flores, J. B. French, P. A. Mello, A. Pandey, and S. S. M. Wong, Rev. Mod. Phys. **53**, 385 (1981).
[42] C. E. Porter and R. G. Thomas, Phys. Rev. **104**, 483 (1956).
[43] Y. Kalmykov *et al.*, Phys. Rev. Lett. **96**, 012502 (2006).
[44] Y. Kalmykov, C. Özen, K. Langanke, G. Martínez-Pinedo, P. von Neumann-Cosel, and A. Richter, Phys. Rev. Lett. **99**, 202502 (2007).
[45] P. Ring and P. Schuck, in *The Nuclear Many Body Problem* (Springer, New York, 1980).
[46] G. Rusev *et al.*, AIP Conf. Proc. **1099**, 799 (2009).
[47] C. T. Angell, S. L. Hammond, H. J. Karwowski, J. H. Kelley, M. Krtička, E. Kwan, A. Makinaga, and G. Rusev, Phys. Rev. C **86**, 051302(R) (2012).
[48] R. Raut, A. Banu, C. Iliadis, J. H. Kelley, G. Rusev, R. Schwengner, A. P. Tonchev, and W. Tornow, J. Phys: Conf. Ser. **337**, 012048 (2012).
[49] D. Savran, M. Fritzsche, J. Hasper, K. Lindenberg, S. Müller, V. Yu. Ponomarev, K. Sonnabend, and A. Zilges, Phys. Rev. Lett. **100**, 232501 (2008).
[50] D. Savran *et al.*, Phys. Rev. C **84**, 024326 (2011).
[51] A. P. Tonchev, S. L. Hammond, J. H. Kelley, E. Kwan, H. Lenske, G. Rusev, W. Tornow, and N. Tsoneva, Phys. Rev. Lett. **104**, 072501 (2010).
[52] F. Hofmann and H. Lenske, Phys. Rev. C **57**, 2281 (1998).
[53] V. G. Soloviev, *Theory of Complex Nuclei* (Pergamon, Oxford, 1976).
[54] M. Grinberg and C. Stoyanov, Nucl. Phys. A **573**, 231 (1994).
[55] S. Volz, N. Tsoneva, M. Babilon, M. Elvers, J. Hasper, R.-D. Herzberg, H. Lenske, K. Lindenberg, D. Savran, and A. Zilges, Nucl. Phys. A **779**, 1 (2006).
[56] M. Urban, Phys. Rev. C **85**, 034322 (2012).
[57] A. J. Koning, S. Hilaire, and M. C. Duijvestijn, AIP Conf. Proc. **769**, 1154 (2005).
[58] M. Beard, S. Frauendorf, B. Kämpfer, R. Schwengner, and M. Wiescher, Phys. Rev. C **85**, 065808 (2012).